Eyewall Replacement Cycles as a Structural Driver of the Bimodal Distribution of Tropical Cyclone Lifetime Maximum Intensity

Elliott Fosler-Lussier[1] and Yuqing Wang[2*]

[1]Department of Atmospheric Sciences, School of Ocean and Earth Science and Technology, University of Hawaii at Manoa, Honolulu, HI 96822

[2]Depatment of Atmospheric Sciences and International Pacific Research Center, School of Ocean and Earth Science and Technology, University of Hawaii at Manoa, Honolulu, HI 96822

July 21, 2025 (submitted)
September 23, 2025 (first revision)
October 14, 2025 (second revision)
Dateline

Key Points:

- TCs that undergo eyewall replacement cycles (ERCs) contribute greatly to the secondary peak in the bimodal distribution of TC LMI.
- Reintensifying ERC TCs occur over higher SST with greater ocean heat content and lower vertical wind shear, reaching extremely high LMIs.
- Rapid intensification drives storms through mid-intensities, while ERCs determine the shape and upper tail of the high intensity peak.

Submitted to ***Geophysical Research Letters***

*Corresponding author: Prof. Yuqing Wang
yuqing@hawaii.edu

Abstract: Tropical cyclone (TC) lifetime maximum intensity (LMI) exhibits a distinct bimodal distribution, with peaks at tropical storm and major hurricane strength. Using a best-track-based algorithm to identify eyewall replacement cycle (ERC) storms, we show that ERC storms overwhelmingly populate the high-intensity peak. Both reintensifying and non-reintensifying ERC storms contribute, but those unable to reintensify cluster near 120–140 kt, defining the secondary peak. In contrast, reintensifying ERC storms can achieve higher intensities when moving over warmer seas with greater ocean heat content and reduced vertical wind shear. The scarcity of storms at intermediate intensities (85–105 kt) arises from rapid intensification, which drives systems quickly through this range. These results clarify that while rapid intensification explains the trough at mid-intensities, ERCs, by halting or enabling further strengthening, shape the high-intensity peak and its upper tail. Incorporating ERC dynamics into intensity statistics may improve understanding and prediction of TC extremes.

Key words: Tropical cyclones, lifetime maximum intensity, eyewall replacement cycle, bimodal distribution

Plain Language Summary: Tropical cyclones (TCs) are powerful storms whose strongest winds, called the lifetime maximum intensity (LMI), tend to cluster at two different levels: many storms peak only as tropical storms, while others become major hurricanes. In this study, we show that a key structural process, known as an eyewall replacement cycle (ERC), largely explains this "two-peak" pattern. An ERC occurs when a storm's inner eyewall is replaced by a new, outer eyewall. Using a new detection method applied to best-track data, we found that nearly all storms with ERCs fall into the higher-intensity group. Those that fail to strengthen again after the ERC typically peak around 120–140 kt, producing the secondary peak in the distribution. In contrast, storms that re-intensify after an ERC can reach greater intensities if they pass over warmer oceans with high heat content and encounter weak vertical wind shear. The relative lack of storms at mid-range intensities (85–105 kt) is explained by rapid intensification, which pushes storms quickly through this range. These results show that ERCs play a central role in shaping the statistics of the strongest tropical cyclones and underscore the value of identifying ERCs to improve intensity forecasts.

1. Introduction

Tropical cyclones (TCs) are among the most destructive weather systems in the tropics, exhibiting substantial variation in intensity, structure, and lifetime. Despite improvements in track forecasting, predicting TC intensity remains a persistent challenge. One particularly intriguing feature is the observed bimodal distribution (probability distribution function – PDF) in lifetime maximum intensity (LMI), which refers to the peak 1-minute sustained wind speed attained by a TC during its lifetime (Lee et al., 2016). Most storms reach either low (tropical storm) or high (major hurricane) intensities, while relatively fewer attain intermediate intensities.

Previous studies have attributed this bimodality to several distinct mechanisms. Soloviev et al. (2014) observed that the secondary peak in the LMI distribution, along with the intervening minimum, aligns with a local minimum and maximum, respectively, in their parameterized surface drag coefficient. They proposed that drag coefficient variability may influence the LMI bimodality. Lee et al. (2016) emphasized the role of rapid intensification (RI), showing that non-RI storms exhibit a unimodal peak near tropical storm intensity, whereas the secondary high-intensity peak emerges only when RI storms are included. More recently, Song et al. (2018) and Xiang et al. (2025) reported a strengthening of this bimodality, linked to increasing global sea surface temperatures and greater variability in storm intensity.

Because eyewall replacement cycles (ERCs) are a distinct phase in many intense TCs, we hypothesize that they may underlie the secondary peak at high intensities. During an ERC, a concentric outer eyewall forms and gradually replaces the original inner eyewall, usually inducing a temporary weakening of the storm followed by potential reintensification (Willoughby et al., 1982; Sitkowski et al., 2011). This process is often marked by an abrupt outward jump in the radius of maximum wind (RMW) (Kossin & Sitkowski, 2009; Yang et al., 2024; Jiang & Wang, 2024). ERCs become increasingly frequent in stronger storms: in the North Atlantic, the probability of ERC rises from below 5% in Category 1 storms to over 50% in Category 5 hurricanes (Kossin & Sitkowski, 2009), with even higher rates observed in the western North Pacific (Kuo et al., 2009; Yang et al., 2013, 2021).

Although previous work has elucidated the processes leading up to LMI, it has largely overlooked how structural transitions, specifically ERCs, might shape the LMI distribution. Because intense storms that develop a secondary eyewall have typically already undergone RI (Fischer et al., 2020; Currier et al., 2024), ERCs are often viewed as interruptions to that intensification and as limits on a storm's ultimate intensity. In this way, ERCs may act to suppress the secondary peak on the high-intensity side of the observed bimodal LMI distribution.

In this study, we examine how ERCs influence the observed bimodal distribution of TC LMI. We analyze both the frequency of ERCs and post-ERC evolution, particularly whether storms reintensify after an ERC, and their impact on the populations of intermediate- and high-intensity storms. We demonstrate that RI is a major driver of the minimum at intermediate intensities, whereas ERCs predominantly control the secondary peak at high intensities, with storms that can reintensify out of an ERC pushing the secondary peak to higher intensities. By linking storm structural dynamics with statistical intensity distributions, our results provide new insights into the drivers of the bimodal LMI distribution and underscore the pivotal role of ERCs in TC intensity forecasting.

2. Data and methods

2.1 Datasets

This study employs several datasets to characterize TC intensity, structure, and environmental variables. Storm position, 10-m maximum sustained wind speed, and radius of maximum wind (RMW) were obtained from the International Best Track Archive for Climate Stewardship (IBTrACS; Knapp et al., 2010; Gahtan et al., 2024). We analyze the influence of ERCs on the LMI distribution over the period 1 July 2001–2023, which corresponds to the period of globally consistent RMW estimates (Landsea & Franklin, 2013), excluding 2004 due to incomplete RMW data.

Environmental variables were drawn from the Statistical Hurricane Intensity Prediction Scheme (SHIPS) archive (DeMaria et al., 2005). Because SHIPS records are available only for

2002–2003 and 2005–2021 globally, and from 1 July 2001 onward for the western North Pacific, our environmental analysis is limited to these intervals. From SHIPS we extract sea surface temperature (SST), vertical wind shear (VWS), mid-level relative humidity (RH), oceanic heat content (OHC), and maximum potential intensity (MPI). We also compute the fractional MPI (FMPI), the ratio of a storm's instantaneous intensity to its theoretical MPI, which serves as a proxy for how close a storm is to its thermodynamic ceiling and thus its capacity for reintensification after the ERC.

To calibrate and validate our ERC detection, we rely on an independent dataset of secondary eyewall formation (SEF) events in western North Pacific TCs during 1999–2020, derived from microwave satellite imagery (Wang et al., 2025). This SEF catalog guided the development and tuning of our best-track-based ERC algorithm (Section 2.2).

2.2 Methods

ERCs represent structural transitions in TCs typically identified via high resolution satellite or microwave imagery. Because such imagery is not available uniformly across basins or through historical records, we developed a best-track RMW-based detection algorithm to perform long-term analysis across all TC basins. This approach is justified by the fact that ERCs almost invariably produce an abrupt jump in the RMW as the outer eyewall becomes dominant (Kossin & Sitkowski, 2009; Yang et al., 2024; Jiang & Wang, 2024). Algorithm design and tuning were guided by a curated SEF dataset for western North Pacific storms (Wang et al., 2025).

Our algorithm first finds each instance where the RMW increases between consecutive 6-hour points in the best-track file. Our ERC detection procedure applies five filters to the best-track RMW time series. To be considered an ERC case by the algorithm the RMW increase must feature: 1) an intensity dependent RMW increase between the two consecutive data points of ≥15 nm for storms with winds of 65–75 kt at the point of RMW increase, ≥10 nm for 80–95 kt, and ≥5 nm for ≥100 kt; 2) no intensification in the points prior to the RMW increase of >5 kt/6h or 10 kt/12h for storms with winds of ≤95 kt at the point of RMW increase, (and >10 kt/6h or 15 kt/12h for ≥100 kt storms), since ERCs rarely coincide with strong intensification phases; 3) ≥65 kt winds at the time of the

RMW increase, in line with prior SEF studies; 4) the RMW jump occurring within 30° latitude of the equator to exclude extratropical transition cases; and 5) a minimum distance of 200 km from land, excluding SEF cases that fail to complete ERC before landfall and terrain-induced RMW fluctuations. This algorithm captures the hallmark RMW signature of ERCs while minimizing false positives from rapid intensification or extratropical processes.

To validate the algorithm, each SEF event in the Wang et al. (2025) reference dataset occurring within the RMW best-track dataset's bound of 2001–2003 and 2005–2020 was manually reviewed and assigned as either an ERC case or a non-ERC case, with the latter being done in cases where the storm was too close to land to complete an ERC. The remainder of the storms within the dataset's period that were not listed as SEF storms in the microwave-based dataset were also reviewed via geostationary imagery. Several storms with clear ERC signatures were assigned as ERC cases, while the rest remained non-ERC cases. It was found that of the 275 total storm cases in the SEF dataset, our algorithm correctly identified 152 non-ERC cases and 102 ERC cases, with 8 non-ERC cases being incorrectly identified as having an ERC and 13 ERC cases being missed by our algorithm, which we will call false ERC and false non-ERC cases. We then assessed the algorithm's performance using accuracy, precision and recall, which are defined as follows:

$$Accuracy = \frac{(True\ ERC + True\ Non\ ERC)}{(All\ Cases)} \tag{1}$$

$$\mathrm{Pr}\,e\,cision = \frac{(True\ ERC)}{(True\ ERC + False\ ERC)} \tag{2}$$

$$Recall = \frac{(True\ ERC)}{(True\ ERC + False\ Non{-}ERC)} \tag{3}$$

Our algorithm produced accuracy, precision and recall values of 0.924, 0.927, and 0.887 respectively, suggesting that our algorithm is acceptable. After computing the fraction of storms in each Saffir-Simpson Hurricane Wind Scale category that underwent ERC, it was found that our algorithm suggested a slightly higher albeit comparable ERC frequency to that given by Huang et al. (2023) for all five intensity categories. This is deemed reasonable, as Huang et al. (2023) suggested that a dataset incorporating cases identified by geostationary imagery would include more storms than one solely utilizing microwave imagery, which is capable of missing shortduration ERC events. Although there remains some inconsistency between our adjusted dataset and the best-track-based dataset, the metrics suggest our best-track-based algorithm provides a reasonable representation of the set of ERC storms.

In our analysis, storms flagged as Category E (ERC cases) were further divided based on their post-ERC intensity evolution. Category EI (ERC, intensifying) includes storms that reintensified after an ERC, whereas Category ED (ERC, decaying) comprises storms that did not. To elucidate different evolutionary pathways, we subdivided Category EI into two timing-based groups: Category EIB (ERC, Intensifying, before LMI) where the first ERC occurred before the storm reached its LMI, and Category EIA (ERC, intensifying, after LMI) where the first ERC occurred after the storm attained its LMI.

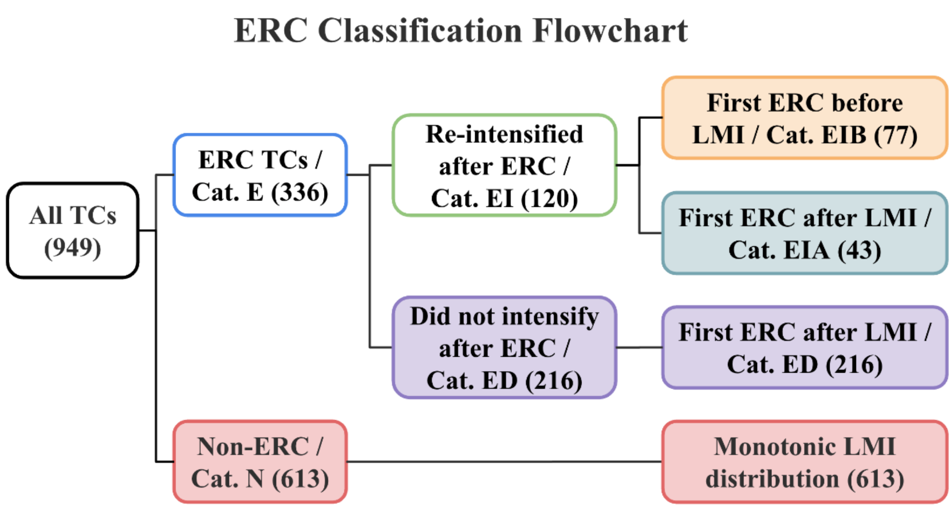

Figure 1. Flowchart showing the storm classification scheme used in this study. The number of storms in each category within the LMI dataset is given in parentheses.

We also defined two additional pairings to examine environmental influences across the LMI spectrum and varying reintensification potentials. By FMPI at the completion of ERC, we considered EIL (ERC, intensifying, low FMPI) and EDL (ERC, decaying, low FMPI) for FMPI<0.7 (storms well below their thermodynamic limit), and EIH (ERC, intensifying, high FMPI) and EDH (ERC, decaying, high FMPI) for FMPI≥0.7 (storms approaching their thermodynamic ceiling). By LMI bin, we considered low LMI<85 kt (primary peak in the LMI probability density), medium LMI 85–105 kt (local trough in the LMI distribution), and high LMI>105 kt (secondary peak in the LMI distribution). This scheme allows us to isolate how ERC timing, thermodynamic state, and ultimate storm intensity jointly govern post-ERC evolution.

Figure 1 summarizes all major classification categories. These groupings enable a systematic evaluation of the environmental conditions and evolutionary pathways associated with each ERC type, offering new insights into the processes that shape the LMI distribution.

3. Results

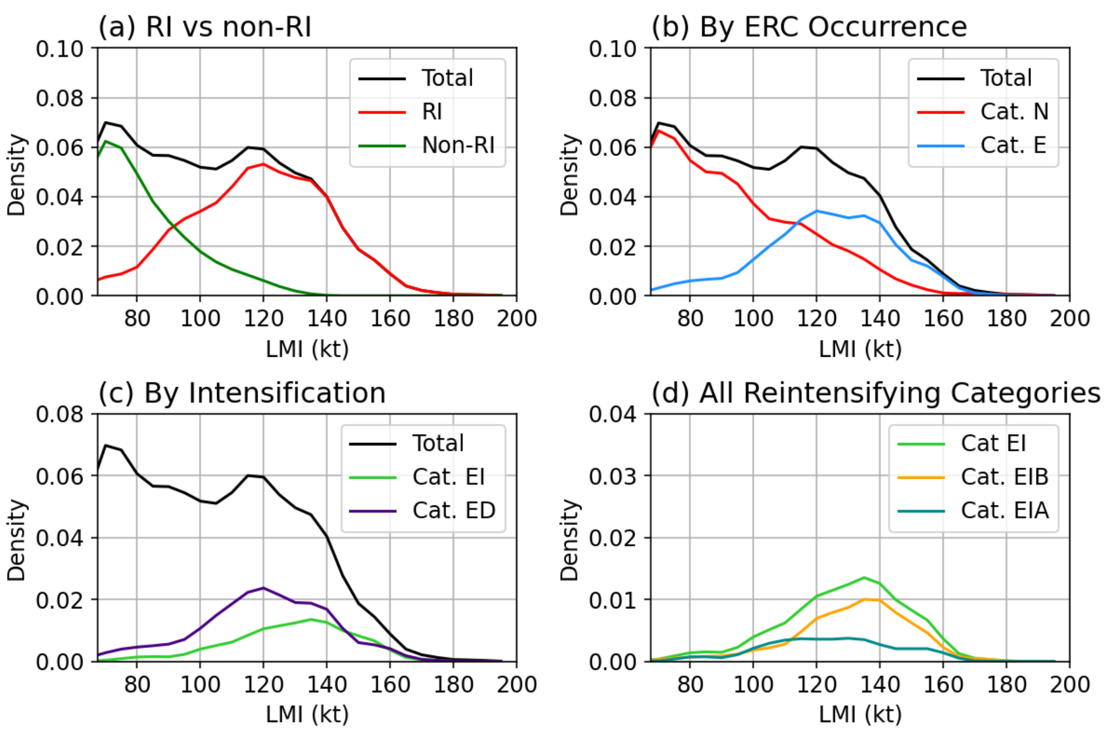

Figure 2. Components of the LMI probability density function (PDF): (a) all storms, RI and non-RI subsets; (b) all storms, ERC (E) and non-ERC (N) subsets; (c) ERC storms divided into reintensifying (EI) and non-reintensifying (ED) cases; and (d) EI storms subdivided into those undergoing ERC before (EIB) and after (EIA) LMI. The dataset includes 2001–2023 globally, plus the second half of 2001 in the western North Pacific. RI is defined as ≥35 kt/24 h following Lee et al. (2016). All curves are smoothed using a 5-bin weighted moving average.

Figure 2a reaffirms the bimodal structure of the LMI probability density function (PDF), with pronounced peaks at both low and high intensities, consistent with earlier findings (Lee et al., 2016; Song et al., 2018; Xiang et al., 2025). In good agreement with Lee et al. (2016), rapid intensification

(RI) storms in our dataset show a strong connection with the secondary LMI peak. Because many ERC storms undergo RI prior to secondary eyewall formation, it is not surprising that ERC storms (Category E) contribute to the secondary peak and the higher intensities in the LMI distribution (Figure 2b). By contrast, non-ERC storms (Category N), like non-RI storms, dominate the lower-intensity peak.

Further disaggregation of Category E storms shows that both reintensifying (Category EI) and non-reintensifying (Category ED) cases contribute to the secondary LMI peak (Figure 2c). ED storms peak near 120 kt, decrease gradually toward 140 kt, and drop off rapidly thereafter, closely matching the LMI distribution around the secondary peak in Figure 2b. This indicates that ED storms contribute more strongly to the secondary peak than EI storms, whose LMI peaks around 135 kt. These results demonstrate that the ERC process interrupts RI and prevents storms from reaching higher intensities. Splitting EI storms into those experiencing their first ERC before LMI (Category EIB) versus after LMI (Category EIA) reveals that EIB storms dominate the EI distribution, peaking near 135 kt and tapering gradually at higher intensities. In contrast, relatively few storms undergo ERC after their LMI (EIA). This suggests that reintensification after ERCs is critical in enabling storms to achieve higher LMIs, and identifying the key factors that support post-ERC reintensification is therefore essential.

We first compared environmental parameters at each storm's LMI between ERC (Category E) and non-ERC (Category N) cases. Mean MPI was modestly higher for ERC storms (133.9 kt) than for non-ERC storms (128.6 kt) (Figure 3a). The abundance of high MPI, non-ERC cases likely reflects regions with dense storm tracks, such as the Philippine Sea, Caribbean Sea, and Gulf of Mexico, where storms often make landfall before an ERC can occur. Fractional MPI (FMPI) values were even more divergent: ERC storms were strongly skewed toward FMPI=0.8–1.0, indicating that they frequently approach their theoretical thermodynamic limit (Figure 3b).

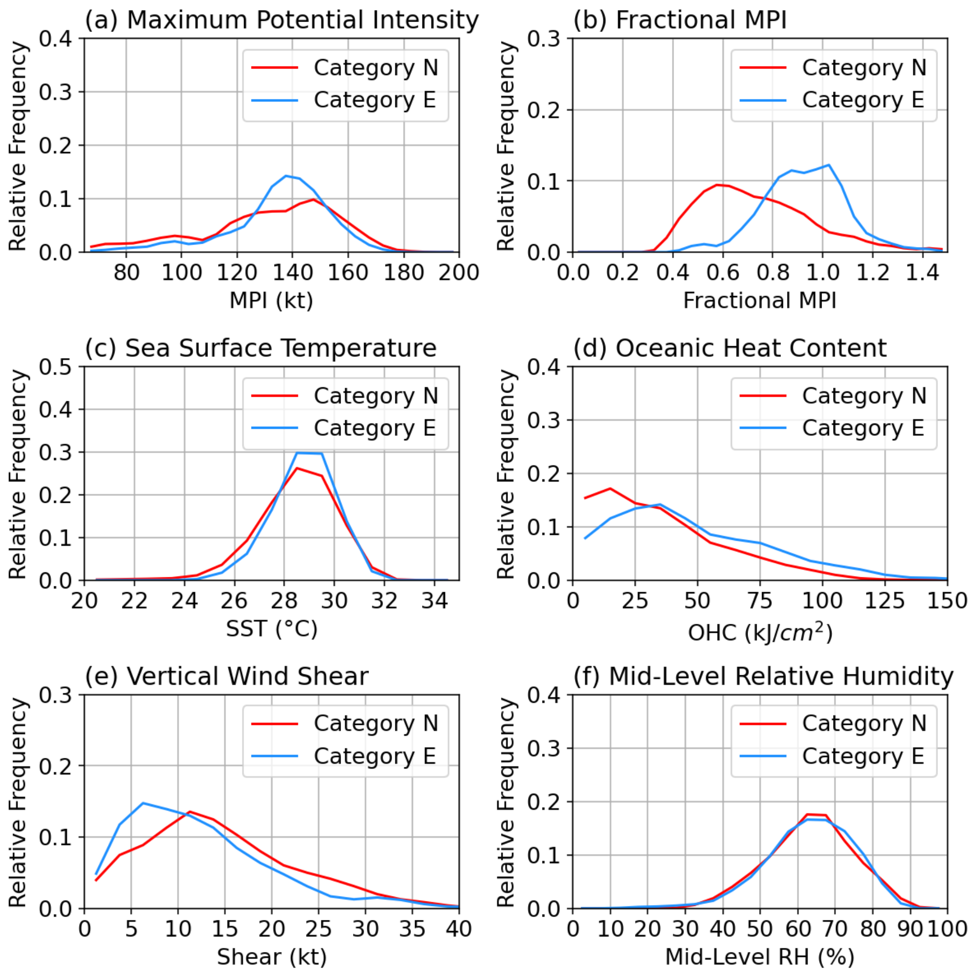

Figure 3. Probability density functions of environmental variables at the time of LMI for non-ERC (N) and ERC (E) storms. Variables shown are: (a) MPI, (b) fractional MPI, (c) SST, (d) ocean heat content (OHC), (e) vertical wind shear (VWS), and (f) midlevel relative humidity (RH). Distributions are smoothed using a 3-bin weighted average.

Other environmental variables at LMI showed smaller but statistically significant differences. Mean SST and midlevel RH were similar between categories (~28.4–28.7°C and ~62.6–62.8%, respectively), but ERC storms experienced substantially higher OHC (~46 vs. 32 kJ cm^{-2}) and lower vertical wind shear (~12 vs. 14.5 kt) (Figures 3c–3f). Student's T-tests (α=0.05) confirm that MPI, FMPI, SST, OHC, and shear differ significantly between ERC and non-ERC groups, underscoring the role of enhanced thermodynamic and reduced shear environments in facilitating ERCs.

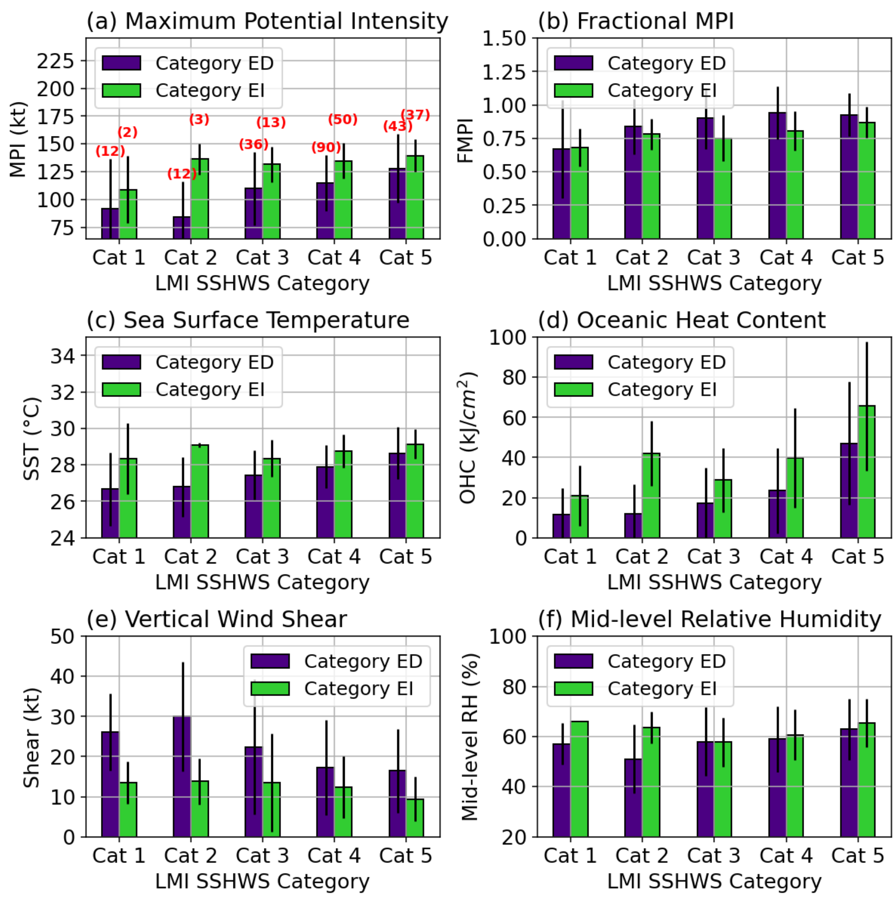

Figure 4. Mean (bars) and one standard deviation (lines) of potential intensity and environmental variables at the completion of ERC for ED and EI storms. Variables include: (a) MPI, (b) fractional MPI, (c) SST, (d) OHC, (e) VWS, and (f) midlevel RH. Outlier FMPI values >1.5 were omitted. The number of cases in each LMI category is indicated in (a).

To evaluate post-ERC reintensification potential, we compared environmental parameters at the time of completion of ERC between the reintensifying (Category EI) and non-reintensifying (Category ED) storms. Category EI storms exhibited narrower MPI distributions (Figure 4a) and FMPI values predominantly in the 0.6–0.8 range, conditions conducive to further intensification. By contrast, many Category ED storms clustered near FMPI=1.0, indicating they had effectively reached their thermodynamic ceiling and lacked the potential for additional strengthening (Figure 4b).

Environmental contrasts at the completion of ERC were even more pronounced than those at the time of LMI. Category EI storms had higher SSTs (mean 28.8°C vs. 27.8°C, Figure 4c), nearly twice the OHC (47.2 vs. 26.1 kJ cm^{-2}, Figure 4d), lower wind shear (11.5 vs. 19.4 kt, Figure 4e), and slightly higher RH (62.1% vs. 59.0%, Figure 4f) compared to Category ED, with reintensification being consistently associated with more favorable conditions through all intensity ranges. These results emphasize the role of environmental favorability in supporting reintensification after the ERC. Three of the four environmental variables differed significantly between the Category ED and EI groups, with P-values on the order of 10^{-8} to 10^{-10} for SST, OHC and shear, while the RH difference was marginally significant (p=0.033). It should be noted that a limited sample size may limit the robustness of generalizations for these groups, particularly for Category EI storms below Category 3 intensity, only 6 such cases had LMIs below this strength.

Subgrouping by FMPI highlights further contrasts. Storms in the low FMPI category (EIL; FMPI<0.7) experienced markedly more favorable environments than their non-reintensifying peers (EDL), with higher SSTs (~28.9°C), greater OHC (~41.2 kJ cm^{-2}), lower shear (~15 kt), and elevated RH (~62.6%). Notably, even among high FMPI cases (EIH vs. EDH), reintensification occurred under exceptional conditions: EIH storms exhibited the highest OHC and the lowest shear of all four FMPI-based subgroups, demonstrating that strong thermodynamic and shear environments can overcome the proximity to the MPI ceiling.

Finally, stratifying by LMI bins reveals how environmental constraints shape the bimodal PDF. Low LMI (<85 kt) storms occur in marginal, highly unfavorable environments. In the medium LMI (85–105 kt) range, which corresponds to the PDF's trough, storms are scarce and still face unfavorable but less hostile conditions than those in the low LMI range. Conversely, high LMI (>105 kt) storms consistently experience the most supportive environments, whether they reintensify or simply sustain their peak intensity for ERC storms. These contrasts underscore that the LMI bimodality reflects distinct environmental limitations across intensity regimes.

TCs that undergo ERCs tend to be intense and often experience RI prior to eyewall replacement. Consequently, the secondary peak in the bimodal LMI distribution is statistically linked to both RI and ERC events. Intensification rates typically maximize in the 90–115 kt range (Figure 5), driving storms in this band to intensify further. This explains the trough at intermediate intensities and the emergence of a secondary peak at higher intensities. However, RI alone cannot explain the precise intensity at which the secondary peak occurs. By contrast, ERC storms, especially those that do not reintensify, exhibit a broad peak between 120–140 kt, closely aligned with the secondary maximum in the LMI distribution (Figures 2b,c). This demonstrates that the ERC process interrupts RI and prevents storms from reaching higher intensities, anchoring the secondary peak at lower values than would be expected if RI proceeded without interruption. Thus, while RI establishes the conditions for a secondary peak, its exact shape and upper-tail extension are governed by the distinct evolutionary pathways of ERC storms.

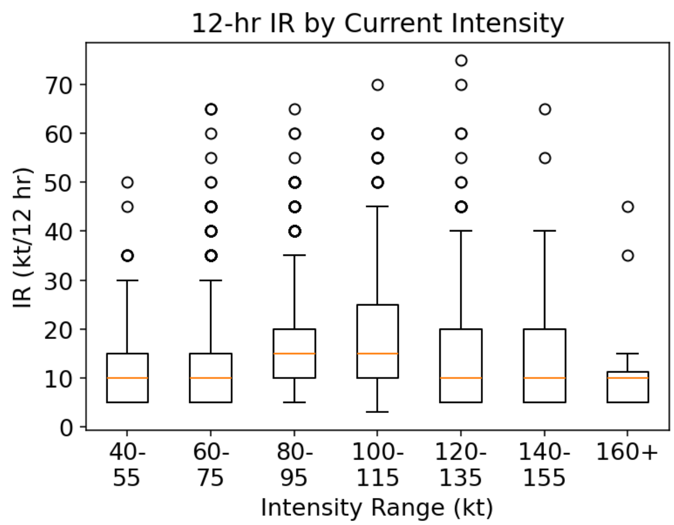

Figure 5. Box-whisker plots of centered 12-hour intensification rates (IRs), grouped by 20-kt intensity bins. Only positive IRs are included. Boxes show the 25th–75th percentiles, whiskers denote the 5th–95th percentiles, and horizontal orange lines mark the medians.

4. Conclusions and discussion

This study provides new insights into the mechanisms shaping the bimodal distribution of TC LMI. By developing and applying a best-track-based algorithm to detect ERCs, we show that these structural transitions are central to the emergence and form of the high-intensity peak. While RI drives storms swiftly through the intermediate 85–105 kt range, ERCs, by halting, sustaining, or permitting renewed strengthening, determine both the placement and the shape of the secondary peak.

Our analysis reveals that both reintensifying (EI) and non-reintensifying (ED) ERC storms cluster at high intensities. ED storms, which fail to strengthen further, tend to peak between 120–140 kt, anchoring the secondary maximum in the LMI distribution. In contrast, EI storms extend the distribution's upper tail by reintensifying after an ERC, with their evolution tightly linked to environmental favorability. Specifically, higher sea surface temperatures, elevated ocean heat content, and reduced vertical wind shear consistently distinguish EI storms from their ED counterparts. Fractional maximum potential intensity further separates storms that are near their thermodynamic limit from those that retain capacity to intensify, offering a useful diagnostic for post-ERC outcomes.

Stratification by intensity bins highlights the distinct physical regimes underlying the bimodality. Low-LMI storms (<85 kt) arise in marginal environments that limit growth. The trough in the 85–105 kt range reflects the fact that storms rarely end their intensification there; both observations and theory (Wang et al., 2021a,b, 2022, 2023; Xu et al., 2022, 2023) show that maximum intensification rates typically occur at intermediate intensities, propelling storms upward. Above this stage, pathways diverge: storms either sustain RI into higher categories or undergo an ERC. Because ERCs become increasingly common as intensity rises, they act as the principal regulator of the high-intensity population. Favorable environments enable post-ERC reintensification, extending the distribution toward the thermodynamic ceiling, while unfavorable environments lock storms near the secondary peak.

These results clarify the complementary roles of RI and ERCs in shaping the LMI probability density function. RI alone explains the trough at mid-intensities, but not the exact placement or gradual decline of the high-intensity peak. ERCs, by interrupting RI and modulating subsequent recovery, provide the structural mechanism needed to reproduce both the secondary maximum and its upper-tail behavior. This perspective helps reconcile earlier studies emphasizing RI thresholds (e.g., Lee et al., 2016) with more recent work documenting increased variability in storm intensities.

Nevertheless, several caveats remain. Our ERC detection is limited by the resolution of best-track RMW data and may miss short-lived or subtle events. Sample sizes are particularly constrained in the intermediate and lower-intensity bins, which limits the robustness of subgroup statistics. Broader and more consistent ERC datasets, including those derived from high-resolution satellite records, will be critical to confirming and extending these findings.

In summary, ERCs emerge as a pivotal structural process governing the distribution of TC maximum intensity. By anchoring the secondary peak and modulating the high-intensity tail, ERCs explain features of the LMI distribution that RI alone cannot. Incorporating ERC dynamics into intensity statistics and forecast models is therefore essential for improving prediction of the most destructive storms and for better anticipating the risks associated with future TC extremes.

Acknowledgments: This research was supported by NSF Grant AGS-1834300 and AGS-2521424.

Open Research

The IBTrACS best-track data used for TC ERC detection in the study are available at Gahtan et al. (2024). The SHIPS datasets used in this study are available at https://rammb2.cira.colostate.edu/research/tropical-cyclones/ships/development_data/

Conflict of Interest Statement

The authors have no conflicts of interest to disclose.

References

Cheung, A. A., Slocum, C. J., Knaff, J. A., & Razin, M. N. (2024). Documenting the progressions of secondary eyewall formations. *Weather and Forecasting, 39 (1)*, 19–40. https://doi.org/10.1175/WAF-D-23-0047.1

Currier, J. W., Jr., & Preston, A. D. (2024). The Pairing of Rapid Intensification Events and Eyewall Replacement Cycles in Tropical Cyclones in the Atlantic Basin from 2015 to 2020. *Atmosphere*, *15 (1)*, 53. https://doi.org/10.3390/atmos15010053

DeMaria, M., Mainelli, M., Shay, L. K., Knaff, J. A., & Kaplan, J. (2005). Further improvements to the statistical hurricane intensity prediction scheme (SHIPS). *Weather and Forecasting*, *20 (4)*, 531–543. https://doi.org/10.1175/WAF862.1

Fischer, M. S., Rogers, R. F., & Reasor, P. D. (2020). The rapid intensification and eyewall replacement cycles of Hurricane Irma (2017). *Monthly Weather Review*, *148*(3), 981-1004. https://doi.org/10.1175/MWR-D-19-0185.1

Gahtan, J., Knapp, K. R., Schreck, C. J., Diamond, H. J., Kossin, J. P., & Kruk, M. C. (2024). International best track archive for climate stewardship (IBTRACS) project, version 4.01. [Dataset]. NOAA National Centers for Environmental Information.

https://doi.org/10.25921/82ty-9e16.

Huang, X., Lu, P., Zhang, B., Lin, Y.-L., & Huang, X.-M. (2023). Transformer aided construction of a long-term tropical cyclone concentric eyewalls dataset. *IEEE Journal of Selected Topics in Applied Earth Observations and Remote Sensing*, 1–9. https://doi.org/10.1109/JSTARS.2023.3281727

Jiang, J., & Wang, Y. (2024). The roles of moat width and outer eyewall contraction in affecting the timescale of eyewall replacement cycle. *Journal of Geophysical. Research–Atmospheres*. *129 (19)*, e2024JD041488, https://doi.org/10.1029/2024JD041488.

Kaplan, J., & DeMaria, M. (2003). Large-scale characteristics of rapidly intensifying tropical cyclones in the north Atlantic basin. *Weather and Forecasting, 18 (6)*, 1093–1108. https://doi.org/10.1175/1520-0434(2003)018<1093:LCORIT>2.0.CO;2

Knapp, K. R., Kruk, M. C., Levinson, D. H., Diamond, H. J., & Neumann, C. J. (2010). The international best track archive for climate stewardship (IBTRACS): Unifying tropical cyclone best track data. *Bulletin of the American Meteorological Society, 91 (3)*, 363–376. https://doi.org/10.1175/2009BAMS2755.1

Kossin, J. P., Olander, T. L., & Knapp, K. R. (2013). Trend analysis with a new global record of tropical cyclone intensity. *Journal of Climate, 26 (24)*, 9960–9976. https://doi.org/10.1175/JCLI-D-13-00262.1

Kossin, J. P., & Sitkowski, M. (2009). An objective model for identifying secondary eyewall formation in hurricanes. *Monthly Weather Review, 137 (3)*, 876–892. https://doi.org/10.1175/2008MWR2701.1

Kuo, H.-C., Chang, C.-P., Yang, Y.-T., & Jiang, H.-J. (2009). Western North Pacific Typhoons wit h Concentric Eyewalls. *Monthly Weather Review*, *137*(11), 3758-3770. https://doi.org/10.117 5/2009MWR2850.1

Landsea, C. W., & Franklin, J. L. (2013). Atlantic hurricane database uncertainty and presentation of a new database format. *Monthly Weather Review, 141 (10)*, 3576–3592. https://doi.org/10.1175/MWR-D-12-00254.1

Lee, C.-Y., Tippett, M. K., Sobel, A. H., & Camargo, S. J. (2016). Rapid intensification and the bimodal distribution of tropical cyclone intensity. *Nature communications, 7 (1)*, 10265. https://doi.org/10.1038/ncomms10625

Sitkowski, M., Kossin, J. P., & Rozoff, C. M. (2011). Intensity and structure changes during hurricane eyewall replacement cycles. *Monthly Weather Review, 139 (12)*, 3829–3847. https://doi.org/10.1175/MWR-D-11-00034.1

Soloviev, A. V., Lukas, R., Donelan, M. A., Haus, B. K., & Ginis, I. (2014). The air sea interface and surface stress under tropical cyclones. *Scientific reports, 4 (1)*, 5306. https://doi.org/10.1038/srep05306

Song, J., Klotzbach, P. J., Tang, J., & Wang, Y. (2018). The increasing variability of tropical cyclone lifetime maximum intensity. *Scientific reports, 8 (1),* 16641. https://doi.org/10.1038/s41598-018-35131-x

Wang, Y.-F., Qiu, X., & Tan, Z.-M. (2025). Investigating the environmental characteristics of intense tropical cyclones with concentric eyewalls over the western north pacific. *Monthly*

Weather Review, 153 (4), 717–733. https://doi.org/10.1175/MWR-D-24-0091.1

Wang, Y., Li, Y., Xu, J., Tan, Z.-M., & Lin, Y. (2021a). The intensity dependence of tropical cyclone intensification rate in a simplified energetically based dynamical system model. *Journal of the Atmospheric Sciences, 78 (7)*, 2033–2045. https://doi.org/10.1175/JAS-D-20-0393.1

Wang, Y., Li, Y., & Xu, J. (2021b). A new time-dependent theory of tropical cyclone intensification. *Journal of the Atmospheric Sciences, 78 (12)*, 3855–3865. https://doi.org/10.1175/JAS-D-21-0169.1

Wang, Y., Xu, J., & Tan, Z.-M. (2022). Contribution of dissipative heating to the intensity-dependence of tropical cyclone intensification. *Journal of the Atmospheric Sciences*, *79 (8)*, 2169–2180. https://doi.org/10.1175/JAS-D-22-0012.1

Wang, Y., Tan, Z.-M., & Li, Y. (2023). Some refinements to the most recent simple time-dependent theory of tropical cyclone intensification and sensitivity. *Journal of the Atmospheric Sciences, 80(1)*, 321–335. https://doi.org/10.1175/JAS-D-22-0135.1

Willoughby, H. E., Clos, J. A., & Shoreibah, M. G. (1982). Concentric Eye Walls, Secondary Wind Maxima, and The Evolution of the Hurricane vortex. *Journal of Atmospheric Sciences, 39(2)*, 395-411. https://doi.org/10.1175/1520-0469(1982)039<0395:CEWSWM>2.0.CO;2

Xiang, Q., Zhao, H., Klotzbach, P. J., Su, T., Wang, C., & Wu, L. (2025). Amplified bimodal distribution of western north pacific tropical cyclone lifetime maximum intensity. *Geophysical Research Letters, 52 (2)*, e2024GL111637. https://doi.org/10.1029/2024GL111637

Xu, J., & Wang, Y. (2022). Potential intensification rate of tropical cyclones in a simplified energetically based dynamical system model: an observational analysis. *Journal of the Atmospheric Sciences, 79 (4)*, 1045–1055. https://doi.org/10.1175/JAS-D-21-0217.1

Xu, J., Wang, Y., & Yang, C. (2023). Quantifying the Environmental Effects on Tropical Cyclone Intensity Change Using a Simple Dynamically Based Dynamical System Model. *Journal of the Atmospheric Sciences, 80 (12)*, 2897–2913. https://doi.org/10.1175/JAS-D-23-0058.1

Yang, X.-W., Wang, Y., Wang, H., Xu, J., and Zhan, R.-F. (2024). Effect of the initial vortex structure on intensity change during eyewall replacement cycle of tropical cyclones: A numerical study. *Journal of Tropical Meteorology*, 30 (2), 106–117, https://doi.org/10.3724/j.1006-8775.2024.011

Yang, Y.-T., Kuo, H.-C., Hendricks, E. A., & Peng, M. S. (2013). Structural and intensity changes of concentric eyewall typhoons in the western North Pacific basin. *Monthly Weather Review*, *141*(8), 2632-2648. https://doi.org/10.1175/MWR-D-12-00251.1

Yang, Y.-T., Kuo, H.-C., Tsujino, S., Chen, B.-F., & Peng, M. S. (2021). Characteristics of the long-lived concentric eyewalls in tropical cyclones. *Journal of Geophysical Research: Atmospheres*, *126*(11), e2020JD033703. https://doi.org/10.1029/2020JD033703